On the depth-dependent accuracy of plane-wave based vector velocity measurements with linear arrays

(Article begins on next page)

06 September 2024

On the depth-dependent accuracy of plane-wave based vector velocity measurements with linear arrays

Stefano Rossi, Alessandro Ramalli and Piero Tortoli

Abstract— High-frame-rate vector Doppler methods are used to measure blood velocities over large 2-D regions, but their accuracy is often estimated over a short range of depths. This paper thoroughly examines the dependence of velocity measurement accuracy on the target position. Simulations were carried out on flat and parabolic flow profiles, for different Doppler angles, and considering a 2-D vector flow imaging (2-D VFI) method based on plane wave transmission and speckle tracking. The results were also compared with those obtained by the reference spectral Doppler (SD) method.

Although, as expected, the bias and standard deviation generally tend to worsen at increasing depths, the measurements also show that: (1) the errors are much lower for the flat profile (from $\approx$-4±3% at 20 mm to $\approx$-17±4% at 100mm), than for the parabolic profile (from $\approx$-4±3% to $\approx$-38±%). (2) Only part of the relative estimation error is related to the inherent low resolution of the 2-D VFI method. For example, even for SD, the error bias increases (on average) from -0.7% (20 mm) to -17% (60 mm) up to -26% (100 mm). (3) Conversely, the beam divergence associated to the linear array acoustic lens was found to have great impact on the velocity measurements. By simply removing such lens, the average bias for 2-D VFI at 60 and 100 mm dropped down to -9.4% and -19.4%, respectively.

In conclusion, the results indicate that the transmission beam broadening on the elevation plane, which is not limited by reception dynamic focusing, is the main cause of velocity underestimation in the presence of high spatial gradients.

Index Terms—Vector flow imaging, pulsed wave Doppler, spectral Doppler analysis, plane waves, high frame rate imaging, deep vessels.

I. INTRODUCTION

For a long time, quantitative ultrasound Doppler measurements have been limited to the detection of the axial velocity component (v_z) in a single [1] or in multiple [2], [3] sample volumes aligned along a direction selected by the operator. 2-D vector Doppler methods [4], [5] were introduced to detect a second component of the velocity vector. In most cases, since linear arrays were used, the second component (v_x) corresponded to the one included in the scan (x-z) plane. Most studies were addressed to demonstrate new methods in one [6], [7] or multiple [8], [9] sample volumes covering a short range around a fixed (often shallow) depth. For example, in [6], [9] the investigation was limited to the carotid artery (~15-30 mm

depth), while the paper [8] reported measurements at 70 mm, but none of them assessed the estimation accuracy on a wide range of depths.

Although 2-D vector velocity maps at low time resolution were already presented in the mid '90s [10] and later improved by exploiting transverse oscillations [11], [12], a great boost to 2-D vector flow imaging (2-D VFI) was given by the transmission of broad beams, such as diverging and plane waves [13]–[19]. The simultaneous and uniform insonification of a wide and deep region has in fact encouraged the development of methods to detect the 2-D vector velocity components all over such region. 2-D VFI, based on broad beams transmitted by different array types, has found several application fields, spanning cardiac [20], [21], abdominal [22], [23], and peripheral vascular imaging [24], [25]. In the latter case, although several 2-D VFI methods have been proposed and even discussed in a challenge at the IEEE IUS 2018 meeting [26], not much attention has been paid to the possible dependency of the measurement accuracy on the probe-to-target distance. For multi-angle methods [27]–[29], the accuracy is expected to be worse at the small interbeam angles involved in great depth investigations [30]. On the other hand, the accuracy of plane wave-based velocity estimators and speckle-tracking methods [31]–[36], [24], [25] should be less affected by depth, if not for the unavoidable signal-to-noise (SNR) loss due to attenuation.

In [37], 2-D VFI measurements, based on the transmission of plane waves, were found to be affected by up to 35% underestimation, when investigating a flow placed at several centimeters from a linear array. Since it was observed that the best performance (3% underestimation) was obtained at depths close to the elevation focus of the probe acoustic lens, it was hypothesized that the overall spatial resolution could be responsible, at least in part, for such behavior [38].

This paper extends the work presented in [37], [38] by thoroughly investigating, by means of simulations, the dependence of VFI accuracy on the target depth. Two types of flow velocity profiles, flat and parabolic, in a wall-less tube located at different distances (from 2 to 10 cm) and Doppler angles (90°, 82.5° and 75°) have been considered. The VFI method described in [34] and adopted in [37], [38], was used here, too. It is a classic speckle tracking algorithm that efficiently estimates, in the frequency domain, the displacements within a kernel, and can be considered representative of the class of VFI methods based on the

TABLE I MAIN SIMULATION SETTINGS

Probe Parameters		
Transducer	1-D Linear Array	2-D Circular Grid
Number of active elements	128	804
Pitch (δ_x) [mm]	0.245	0.245×0.245
Element size [mm]	0.215	0.215×0.215
Elevation focus [mm]	18 (Focused lens), Inf (Flat lens)	-
System Parameters		
Speed of sound (c) [m/s]	1540	
Tx central frequency (f_0) [MHz]	6	
Rx sampling frequency (f_c) [MHz]	50	
Axial distance between RF samples (δ_z) [μm]	15.4	
PRF [Hz]	1250	
Blood Flow Parameters		
Inner Radius (R) [mm]	4	
Beam-to-flow angle (ϑ_D) [°]	90, 82.5, 75	75
Flow axis depth (z_0) [mm]	20, 40, 60, 80, 100	
Peak velocity (v_p) [cm/s]	15	
Scatterers density [1/mm3]	25	

transmission of plane waves. The estimated velocity modules were compared with both the ground truth and those detected by the classic spectral Doppler approach, assumed as reference gold standard. Simulation results suggest that the transmitted beam shape plays a role on the mentioned velocity underestimation. This hypothesis is validated by measurements performed by simulating a different acoustic lens for the linear array as well as a 2-D array capable of tailoring the transmission beam on both azimuth and elevation.

The paper is organized as follows: section II details the simulation setup, the array, the used estimation methods, and the performance metrics. The results are described and discussed in section III, while section IV concludes the paper.

II. SIMULATIONS

A. Linear array probe

1) Simulation setup

Simulations, carried out in Matlab©, were based on Field IIpro© [39]. The parameters of the linear array, summarized in Table I, were chosen according to the technical
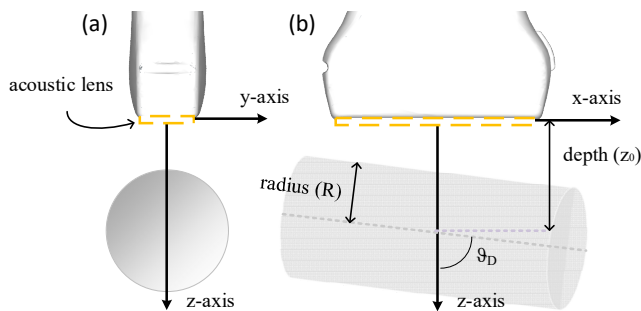

Fig. 1 Reference system y-z plane (a) and x-z plane (b). Note: the vessel axis is parallel to the array surface when ϑ_D=90°.

specifications of a commercial probe (model LA533, Esaote SpA, Florence, Italy). Two versions of the same linear array were simulated: one covered by an acoustic lens focused at 18 mm and the other one covered by an unfocused (flat) lens. Fig. 1 shows the reference system setup.

2) Transmit/receive strategies

The probe elements were excited by 5-cycle sinusoidal bursts at $f_0 = 6\ MHz$, which were time-tapered by a Hamming window. Two transmission schemes were considered:

• Plane wave (PW) transmission: all active elements were simultaneously excited;

• Focused wave (FW) transmission: the elements were excited with delays corresponding to 5 focal depths (20, 40, 60, 80, and 100 mm). The number of linear array transmission elements was modulated to maintain the f-number ≈ 4 in all cases.

In reception, the simulated echo data were sampled at 50 MHz, corresponding to an axial step between consecutive samples (δ_z) of 15.4 μm. For both PW and FW, the number of receiving elements was increased, up to a maximum of 128, to implement a constant f-number (4) through dynamic apodization and keep the lateral resolution constant for a wide range of depths. The radiofrequency (RF) echo-data were beamformed according to the standard delay and sum algorithm for the number of lines needed for each of the two velocity estimation methods described below.

Simulations were conducted for 250 consecutive transmission events, with a pulse repetition frequency (PRF) of 1250 Hz, to cover a total interval of 0.2 s.

3) Numeric phantom

The numeric phantom consisted in a 4-mm inner radius (R), wall-less, cylindrical tube, placed at a distance z_0 of 20, 40, 60, 80, and 100 mm from the probe. Parabolic and flat steady flows, both with 15 cm/s peak velocity, were simulated with a density of 25 scatterers per mm³, which ensures a fully developed speckle in all tested cases. The flow was interrogated at three Doppler angles (ϑ_D= 90°, 82.5° and 75°, see Fig. 1). Ultrasound attenuation and static background tissues were not considered as they would have complicated the already complex simulation setup, with additional variables that could have made harder the interpretation of the results.

4) Flow velocity measurements

Flow velocities were measured according to two different approaches: the first method is representative of the class of 2-D vector velocity estimators based on speckle tracking, while the multigate spectral Doppler (MSD) method, which detects the axial components of the velocity vectors by classic spectral analysis, is assumed as reference. In both cases, the velocity was estimated along the probe axis.

a) Vector velocity estimation

The 2-D high frame rate vector flow imaging method [34] is based on the reconstruction of RF frames following the transmission of PWs. The region of interest is subdivided into rectangles (kernels), whose (z × x) size is 1 × 5 mm. The kernels are weighted by Hann's windows, which halve the equivalent
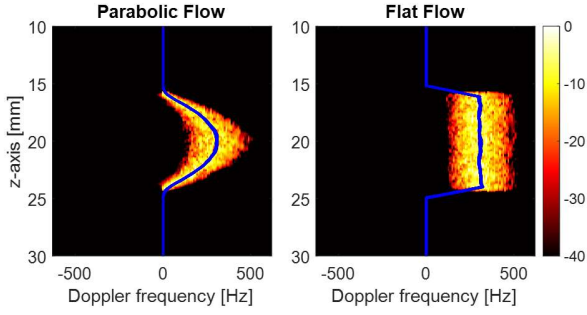
Fig. 2 Example of average MSD frames obtained for parabolic (left) and flat (right) flows around 20 mm depth interrogated with 75° Doppler angle. The spectral amplitudes detected at each depth are reported according to the colormap on the right.
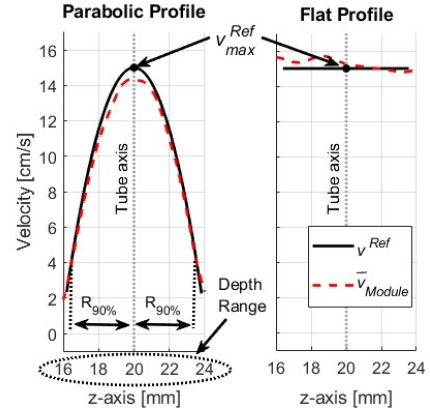

Fig. 3 Example of parabolic (left) and flat velocity profiles (right) estimated by simulations (red dash lines). The reference profiles are represented as solid black lines.

kernel size in both directions. This specific kernel size was chosen to achieve a good compromise between accuracy and spatial resolution [34].

For each kernel, the Δz and Δx displacements were calculated through a 1-D discrete Fourier transform (DFT), and a 2-D DFT, respectively. The spectral phase shifts were first estimated at $n_{f_z}=3$ and $n_{f_x}=10$ frequencies, before being converted to the corresponding displacements (Δ_{zf_m} and $\Delta_{xf_m f_n}$). The velocity components in both directions, v_z and v_x, were estimated as:

$$v_z = \frac{1}{n_{f_z}} \sum_{m=1}^{n_{f_z}} \Delta_{zf_m} \; \delta_z \cdot PRF \qquad (1)$$

$$v_x = \frac{1}{n_{f_z} n_{f_x}} \sum_{m=1}^{n_{f_z}} \sum_{n=1}^{n_{f_x}} \Delta_{xf_m f_n} \delta_x \cdot PRF \qquad (2)$$

Finally, since only steady flow was considered, a low pass finite impulse response filter (order = 80, cutoff frequency = 20 Hz) was applied in the slow-time to smooth the velocity estimates.

b) Multigate Spectral Doppler

The multigate spectral Doppler (MSD) method represents an extension of conventional spectral Doppler to multiple sample volumes aligned along the same scan line [2], [3]. MSD has here been used to provide estimates of the velocity profile detected along the beam axis. The measurements could thus be performed with both PW and FW transmission. In the latter case, the focal depth was made coincident with the vessel axis depth.

After each transmission, MSD processing was applied to the beamformed echo-signals backscattered from K (1300) depths intercepted in fast time at the 50 MHz sampling frequency, sufficient to cover the vessel at both $\vartheta_D = 82.5°$ and $\vartheta_D = 75°$. For each depth, in the slow time direction, the RF analytic signal was weighted with 128-point Hann's windows and converted to frequency by a fast Fourier transform (FFT). While no overlap was considered in the fast-time, a 127-point overlap was empirically set in the slow-time. As an example, Fig. 2 shows the spectral profiles detected for parabolic flow

and flat flow, respectively. In Fig. 2, the vertical axis corresponds to depth and the horizontal axis to the Doppler frequency, while power spectral densities are color-coded according to the colormap on the right.

After 250 transmission events, N_F = 124 MSD frames, each consisting of 128×K pixels, were thus obtained. The averaged spectra were further processed to extract the weighted mean frequency, which was used to estimate the axial velocity component and, finally, the velocity module according to the Doppler equation for the given beam-to-flow angle.

c) Performance metrics

The estimation accuracy and precision were assessed in terms of mean relative bias and standard deviation of the measured velocity values from the center scanline. As proposed in [33], for each depth, z_p, located at a distance from the flow axis shorter than 90% of the pipe radius ($R_{90\%}$ in Fig. 3), the mean relative bias of each estimated velocity module, $v_{Module}(z_p)$, was defined as:

$$\bar{B}_v = \frac{1}{v_{max}^{Ref}} \frac{1}{N_p} \sum_{p=1}^{N_p} \left(\bar{v}_{Module}(z_p) - v^{Ref}(z_p) \right) \qquad (3)$$

where v^{Ref} is the reference velocity module, v_{max}^{Ref} = 15 cm/s is the peak velocity, N_p is the number of selected points and $\bar{v}_{Module}(z_p)$ is the average $v_{Module}(z_p)$ for all frames.

The mean relative standard deviation was calculated as:

$$\bar{\sigma}_v = \frac{1}{v_{max}^{Ref}} \sqrt{\frac{1}{N_p} \sum_{p=1}^{N_p} \sigma_v(z_p)^2} \qquad (4)$$

where:

$$\sigma_v(z_p) = \sqrt{\frac{\sum_{u=1}^{N_F} \left(v_{Module}(z_p, t_u) - \bar{v}_{Module}(z_p) \right)^2}{(N_F - 1)}} \qquad (5)$$

is the standard deviation of the estimated velocity, averaged over the total number of frames, N_F.

B. 2-D array probe

By using the same numeric phantom, blood flow, and system parameters described above, a smaller number of simulations based on a 2-D array was also conducted. The purpose was carrying out a comparative preliminary evaluation of the performance of this class of arrays when measuring velocities at different depths.

A reference 2-D array, having a circular layout with an aperture diameter equal to 7.8 mm, was simulated. It consisted of 804 elements of size 0.215 × 0.215 mm, with pitch 0.245 mm, i.e. the same pitch of the linear probe. Such aperture, dynamically apodized by a Tukey's window, was designed to maintain the RX f-number equal to 4 up to 24 mm (sufficient to include all the vessel when its axis was at 20 mm depth). Keeping the f-number constant for the deeper vessels would have involved an excessive simulation burden with an unrealistic number of active elements.

For this array, simulations were performed with both PW and FW transmission. In the latter case, the focal depths were set coincident with the vessel axis depth, and flow measurements were based on MSD processing.

III. RESULTS AND DISCUSSION

1) Linear array with focused lens

Fig. 4 shows the relative bias and standard deviation of the velocity modules obtained by both velocity estimation methods when flat and parabolic flow profiles, with a $\vartheta_D = 75°$, were insonified by PWs.

This example shows that for the flat flow both methods resulted reasonably accurate at all depths of interest, although MSD performed better than the VFI. When investigating a parabolic flow, the results were still accurate up to 4 cm depth. Specifically, for VFI the bias was <-8.8%, while for MSD it was <-4.8%. However, at greater depths, the performance worsened significantly: although both methods underestimated the velocities, MSD still performed better ($-19.6\% < \bar{B}_{v_{Module}} < -28.4\%$) than VFI
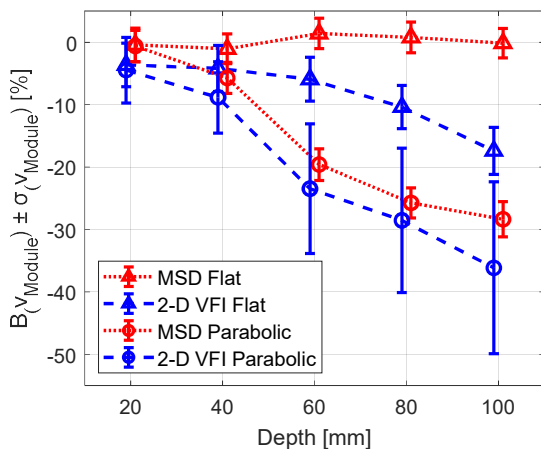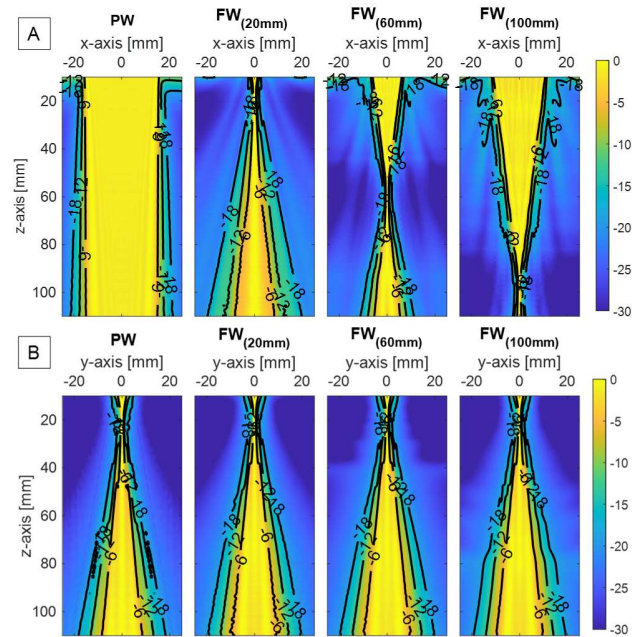

Fig. 5 One-way fields simulated on the x-z plane (A) and y-z plane (B) for a PW and for FWs with focal distances at 20, 60, 100 mm. All fields were normalized by their maximum at each depth.

($-23.5\% < \bar{B}_{v_{Module}} < -36.1\%$). Similar results were obtained for the other settings (see Table II and Table III in the Appendix), highlighting a limited influence of the Doppler angle.

These results suggest that the specific method adopted for the velocity measurements is not the unique source of error determining their deterioration at increasing depths (in fact, two different methods generate similar trends). In particular, the strong underestimation observed for parabolic profiles, but not for flat profiles, reminds the influence of the sample volume size on the detected mean frequencies. In fact the velocities of all particles crossing the sample volume contribute to the velocity estimate, and when the sample volume intercepts a parabolic flow involving a spatial velocity gradient, the Doppler spectrum enlarges ("velocity gradient broadening") and the mean frequency correspondingly decreases [1].

Fig. 4 Relative bias and standard deviaton of velocity estimates obtained with the linear array (including the focused lens) when transmitting plane waves. In this example, ϑ_D was 75° for both parabolic and flat flow profiles. Refer to Table IV and V for numeric values and for the other ϑ_D angles.

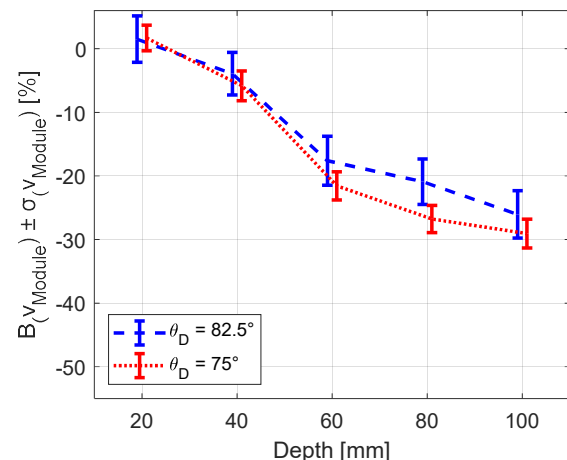

Fig. 6 Relative bias and standard deviaton of MSD velocity estimates obtained with the linear array with focused lens when transmitting FW. In this example parabolic flow was simuated.
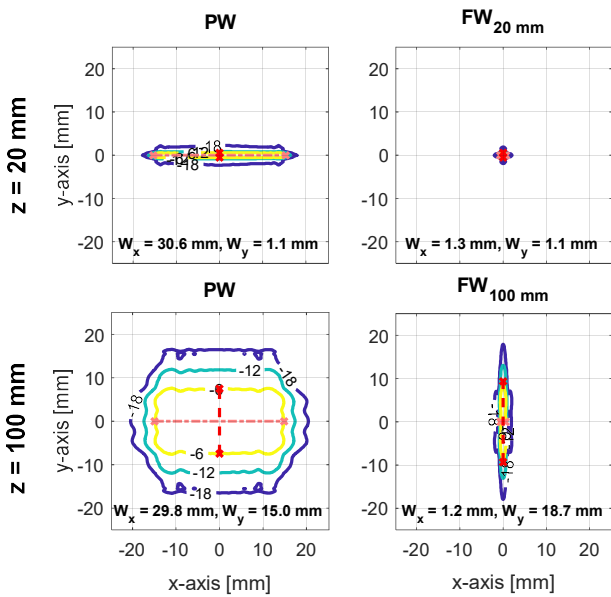
Fig. 7 Beam isolines on planes parallel to the probe surface at 20 mm (top) and 100 mm (bottom) for PW (left) and FW (right) transmissions.

To evaluate the hypothesis that the actual sample volume dimensions turn out to be (at least in part) responsible for the observed behavior, the transmitted (one-way) fields were simulated. The local peak pressure values were calculated on a 1-mm step grid of 51×101 samples over the range [10, 110] mm, along the z-axis, and [-25, 25] mm, along the lateral-axes (either x or y).

Fig. 5 A shows the one-way fields simulated on the (x-z) plane for PW transmission (left) and for FWs with focal distances at 20, 60, and 100 mm. The transmitted PW beam maintains quite a constant width ($w_x \sim 30$ mm) on the lateral direction for all analyzed depths. For the FWs, since the f-number was maintained unchanged, the (-6dB) beamwidth at the focal depths results constant ($w_x = 1.3 \pm 0.1$ mm). These beams might suggest that the larger sample volume in PW transmission may be responsible for the observed depth-dependence of velocity measurements. However, Fig. 6, obtained for FW transmission and MSD processing, confirms that the transmission modality does not significantly influence the results, which are very close to those shown in Fig. 4 and in Table II, obtained in PW mode. This is likely due to the reception dynamic focusing, which similarly reduces the sample volume width in the x-z plane in all cases.

The one-way fields shown in Fig. 5 B, simulated on the elevation plane (y-z) for the same transmission settings, may help in explaining the measurement worsening at increasing depths. It can in fact be observed that differently focusing the beams on the x-z plane does not impact on the beam profile along the y-z plane. The latter one is only affected by the acoustic lens, and, beyond the focal length (18 mm), highlights a progressive broadening due to diffraction. For both focused and plane waves, the beamwidth at -6 dB (w_y), starting from 1.1 mm at 20 mm, reaches 18.7 mm at 100 mm, i.e. with a widening of 1700%. In particular, at 6 cm depth, $w_y = 7.6$ mm, i.e. it is already comparable to the diameter of the simulated vessel (8 mm).
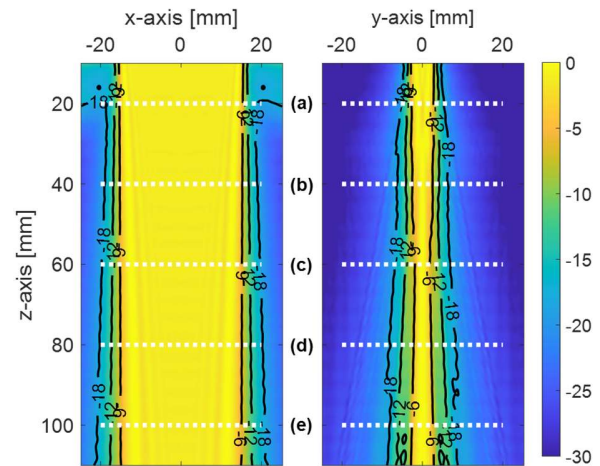

Fig. 8 One-way fields on x-z (left) and y-z (right) planes for the linear array probe with unfocused lens. The fields were normalized by their maximum at each depth.

These observations are confirmed by Fig. 7, which shows the isolines of one-way beams on planes parallel to the array surface at 20 mm and 100 mm depths for both PW and FW transmission. Such plots highlight that, as expected, electronic focusing (right panels) significantly narrows the transmitted beam along the x-direction, but not along the y-direction. The progressive broadening forced by the acoustic lens on the elevation plane yields increasingly wider sample volume regions, which contribute to the received echo signal. Since dynamic focusing is not effective on the y-z plane as in the x-z plane, the behavior of velocity measurements at increasing depths looks consistent with this sample volume enlargement. The tests carried out for the flat flow, which is characterized by a constant velocity distribution over the entire vessel, confirm this hypothesis: there is no spatial velocity gradient here, and the underestimation turns out to be considerably reduced at great depths.

2) Linear array with unfocused lens

Previous considerations can be further corroborated by the simulation of an acoustic lens that produces a less depth-dependent beamwidth. From this point of view, the simplest example is represented by an unfocused lens (e.g. a silicon sheet of uniform thickness). In this case, the one-way fields obtained
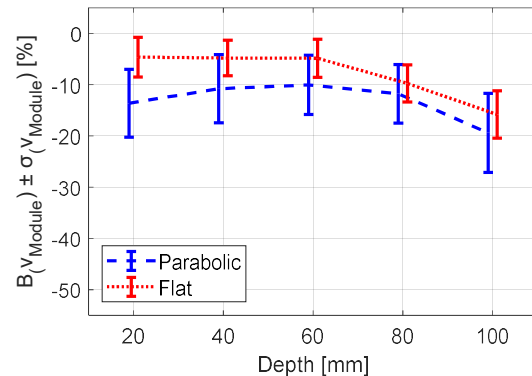

Fig. 9 Relative bias and standard deviaton of 2-D VFI velocity estimates obtained with the linear array including the unfocused lens. In this example, ϑ_D was 75° for both parabolic and flat flow profiles. Refer to Table VI for numeric values at other Doppler angles.

This article has been accepted for publication in IEEE Transactions on Ultrasonics, Ferroelectrics, and Frequency Control. This is the author's version which has not been fully edited and content may change prior to final publication. Citation information: DOI 10.1109/TUFFC.2021.3076284

6
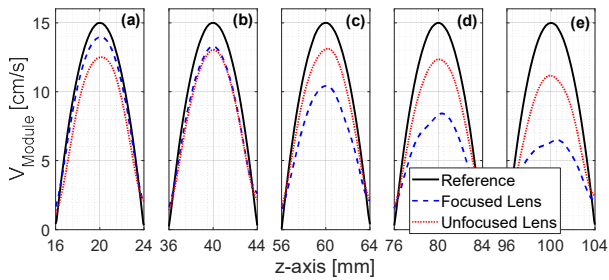
Fig. 10 Modules of the parabolic profiles ($\vartheta_D = 90°$) estimated at 5 depths ((a) 20mm, (b) 40mm, (c) 60mm, (d) 80mm and (e) 100mm), using the focused lens (blue dashed line) and the unfocused one (red dotted line). The ground truth profile is reported in black.

on the lateral and elevation planes for PW transmission, are shown in Fig. 8. The beam on the x-z plane does not differ from that shown for the focused lens and its width is quite constant (30±0.5 mm) at different depths. Instead, the beam significantly differs on the y-z plane: it does not progressively broaden but is more uniform, maintaining a width in the range [3.7, 5.4] mm. The worst resolution is here achieved at 20 mm depth, where, on the contrary, the focused lens performs better.

Fig. 9 shows the bias and standard deviation of the velocity modules estimated when using the 2-D VFI method with an unfocused lens for both parabolic and flat flows at $\vartheta_D = 75°$. The results show that 2-D VFI was reasonably accurate for the parabolic profile (-8.3% < $\bar{B}_{v_{Module}}$ < -19.9%) with the worst performance remaining at 100 mm, consistent with the slight beam enlargement observable in the right panel of Fig.7. Furthermore, the estimates on the flat flow profile (-3.8% < $\bar{B}_{v_{Module}}$ < -17.4%) were similar to those obtained with the focused lens (-3.6% < $\bar{B}_{v_{Module}}$ < -17.4%), as expected in absence of velocity gradients. Numerical results for the other Doppler angles can be found in the appendix in Table IV of the appendix. The latter also reports (Fig. A1) the results of velocity estimations at different depths and SNRs (0, 5, 10 dB). As expected, lower SNRs lead to larger underestimations and wider standard deviations, but the SNR does not impact on the depth-dependent bias trend for both the considered arrays (with and without acoustic lens).

For a direct performance comparison, Fig. 10 shows the velocity profile modules obtained with both focused and unfocused lenses. For the focused lens (blue line), high underestimation is already noted at 60 mm, and it is even more marked at 100 mm. On the other hand, the unfocused lens (red line) allows better estimates at greater depths, although not at 20 mm.

3) 2-D array: preliminary evaluation

Unlike linear arrays, 2-D arrays can control transmission and reception focusing on both azimuth and elevation directions. Hence, if the assumptions of the previous sections are valid, by using this type of probes, the velocity measurements result less depth dependent. Fig. 11 shows the velocity estimates obtained with the circular grid array and the MSD method when observing a parabolic flow with $\vartheta_D=75°$. Although the f-number was here constant only up to 24 mm, the measurement bias is quite depth independent for both FW transmission
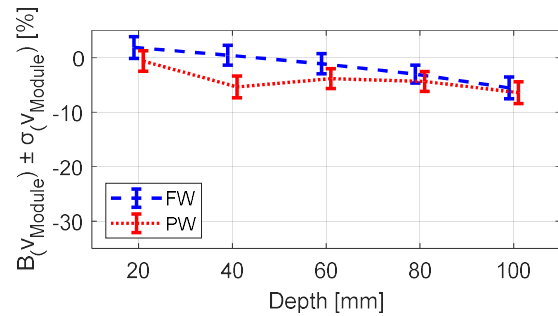

Fig. 11 Relative bias and standard deviaton of MSD velocity estimates obtained with the circular array for FW and PW transmissions. In this example, ϑ_D was 75° for parabolic flow .

($1.9\% < \bar{B}_{v_{Module}}$ < -5.5%) and PW transmission (-0.6% < $\bar{B}_{v_{Module}}$ < -6.4%). Notably, in the latter case, reception dynamic focusing turns out to be sufficient to reduce the sample volume dimensions in all directions, and the measurement errors remain quite low.

4) Sample volume analysis

For each simulated depth, transmission scheme (FW or PW), and probe, the sample volume was estimated as the product of the point spread function (-6dB) widths along the three main directions (x, y, z).

As shown in Fig. 12 A, for the linear array with the focused lens and FW transmission, the sample volume is the smallest
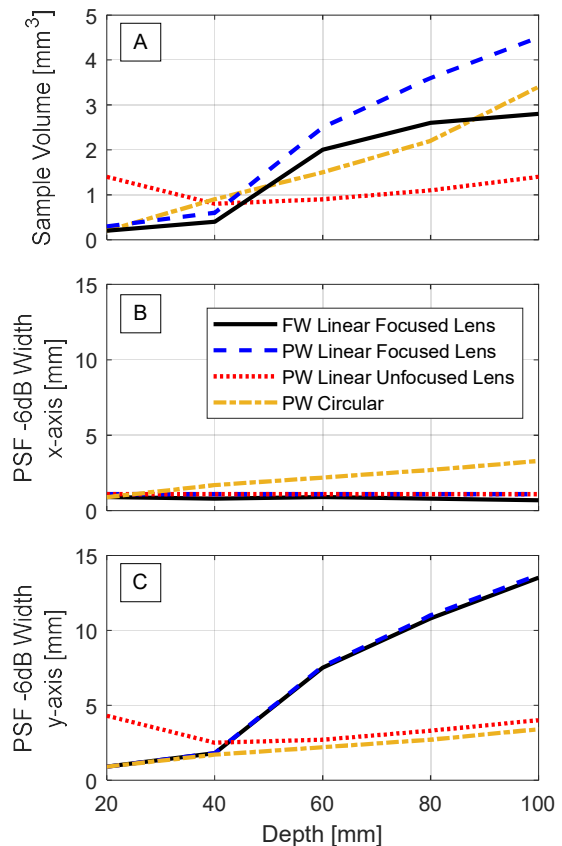

Fig. 12 simulated sample volume size (A), point spread function (-6dB) widths on x-axis (B), and y-axis (C) estimated at different depths for the tested transmission/probe combinations.

(0.2 mm^3) in the proximity of the focal depth but it broadens, up to 14 times (2.8 mm^3), for increasing depths. A similar trend is observed for the PW TX but, as expected due to the lack of TX focusing, the sample volume is generally larger. On the other hand, the sample volume size obtained for the array with the unfocused lens, excited in PW mode, is quite steady at all depths [0.8-1.4] mm^3.

The 2-D circular array showed similar trends for both PW and FW transmissions, and therefore only the one corresponding to PW TX is shown in Fig. 12. The sample volume results very small (0.3 mm^3) at shallow depths but then progressively broadens. This behavior is consistent with the relatively small aperture of the 2-D array, which involves an f-number increasing beyond 20 mm. However, it is worth highlighting that, although the trend is similar to that obtained for the linear array with the focused lens and FW transmission, the impact on the underestimation of the velocity is lower (compare Fig. 6 with Table II and Table III). This lower impact can be ascribed to the symmetrical broadening of the sample volume achieved by the circular array but not by the linear array. Indeed, as shown in panels B and C of Fig. 12, the PSF width of the 2-D array symmetrically broadens, on both axes, from 0.9 mm to 3.4 mm. However, for the 1-D array, the sample volume width is roughly constant [0.7-0.9 mm] on the x-axis (thanks to the constant f-number), but it goes from 0.9 to 13.5 mm on the y-axis. Hence, as the region insonified by the linear array widens with depth, it involves larger underestimations, but this is only due to the broadening on the y-axis, not to the lateral resolution.

IV. SUMMARY AND CONCLUSIONS

Although ultrasound manufacturers offer a variety of probes for different applications, including high-frequency linear arrays with shallow elevation focus for superficial vessels and medium-to-lower-frequency linear arrays with deeper elevation focus for deep vein imaging, the quality of velocity measurements away of the elevation focal area has not been investigated yet.

This work has shown that there is a strict correlation between the shape of the beam produced by an ultrasound linear array and the accuracy attainable by velocity estimates. In particular:

1) Unless a flat profile flow is interrogated, the presence of spatial velocity gradients determines, in general, performance drops with distance from the elevation focus (Fig. 4, Table II, Table III).

2) Such inaccuracy is only partially affected by the used transmission mode: the results obtained by using either PW or FW transmission are quite equivalent (Fig. 4, Fig. 6). For PWs, the lateral size of the sample volume is in fact notably reduced by the reception dynamic focusing.

3) On the other hand, the possible beam broadening on the elevation plane (Fig. 5 and Fig. 7) plays an important role: since, in linear arrays, this is not influenced by dynamic focusing, larger errors are generated from regions where the beam is broader.

4) The great influence of beam broadening on the elevation plane is further confirmed by the more accurate estimates obtained when such broadening is limited, e.g. in linear arrays using an unfocused acoustic lens (Fig. 9, Fig. 10 and Table IV).

5) 2-D arrays are capable of shaping the sample volume in 3-D (Fig. 12). Despite the (typically) small aperture and the limited f-number, they allow keeping the underestimation very low over a large range of depths (Fig. 11). This is particularly important for the possible application of 3-D VFI methods based on the transmission of plane or diverging waves [40]–[43].

6) The chosen velocity estimation method also contributes to the inaccuracy of velocity estimates. For example, the estimates obtained by MSD (Table II) are better than those achieved by 2-D VFI (Table III). This is probably due to the relatively large kernel size needed to estimate the lateral velocity component when speckle tracking-based approaches are used [32]. However, it has to be recalled that spectral-analysis-based velocity estimation methods rely on the knowledge of the Doppler angle [2], [3], which is not a problem in simulations, but determines poor accuracy in *in vivo* applications, when it is assessed manually by the operator.

In conclusion, the results indicate that the transmission beam broadening on the elevation plane, if not limited by reception dynamic focusing, is the main cause of velocity underestimation in the presence of high spatial gradients.

APPENDIX

The following tables show the relative bias and the mean standard deviation of velocity estimates obtained with MSD and probe with focused lens (Table II), 2-D VFI and probe with focused lens (Table III), and 2-D VFI and probe with unfocused lens (Table IV). Fig. A1 shows the results of velocity estimations at different depths and SNRs (0, 5, 10 dB) for both the considered arrays (with and without acoustic lens).

TABLE II *PW TRANSMISSION BY LINEAR ARRAY WITH FOCUSED LENS: RELATIVE BIAS AND MEAN STANDARD DEVIATION OF VELOCITY ESTIMATES BY MULTI GATE SPECTRAL DOPPLER*

Depth [mm]	Flat profile $\overline{B}_{v_{Module}} \pm \overline{\sigma}_{v_{Module}}$ [%]			Parabolic profile $\overline{B}_{v_{Module}} \pm \overline{\sigma}_{v_{Module}}$ [%]		
	$\vartheta_D=90°$	$\vartheta_D=82.5°$	$\vartheta_D=75°$	$\vartheta_D=90°$	$\vartheta_D=82.5°$	$\vartheta_D=75°$
20	-	0.2±4.7	-0.4±2.7	-	-0.8±5.7	-0.6±2.5
40	-	-0.7±5.2	-1±2.4	-	-4.8±4.1	-5.7±2.5
60	-	1.3±5.3	1.4±2.5	-	-14.5±4.3	-19.6±2.5
80	-	1.4±4.4	0.8±2.5	-	-20.3±4	-25.7±2.4
100	-	-1.5±4	-0.1±2.4	-	-24±4	-28.4±2.8

TABLE III *PW TRANSMISSION BY LINEAR ARRAY WITH FOCUSED LENS: RELATIVE BIAS AND MEAN STANDARD DEVIATION OF VELOCITY ESTIMATES BY 2-D VECTOR FLOW IMAGING*

Depth [mm]	Flat profile $\overline{B}_{v_{Module}} \pm \overline{\sigma}_{v_{Module}}$ [%]			Parabolic profile $\overline{B}_{v_{Module}} \pm \overline{\sigma}_{v_{Module}}$ [%]		
	$\vartheta_D=90°$	$\vartheta_D=82.5°$	$\vartheta_D=75°$	$\vartheta_D=90°$	$\vartheta_D=82.5°$	$\vartheta_D=75°$
20	-4.2±3	-3.9±3.2	-3.6±3.5	-3.6±2.5	-4±3.4	-4.5±5.3
40	-4.7±2.7	-4±2.7	-4.2±3.7	-8.9±3.2	-7.1±3.8	-8.8±5.7
60	-4.9±2.4	-5.3±3.1	-5.9±3.5	-22.4±5	-22.1±6.7	-23.5±10.4
80	-10.1±2.8	-10.6±3.2	-10.4±3.5	-31.1±5.2	-31.8±7.4	-28.5±11.6
100	-17.1±2.9	-17±3.5	-17.4±3.8	-37.7±5.7	-36.8±9	-36.1±13.8

This article has been accepted for publication in IEEE Transactions on Ultrasonics, Ferroelectrics, and Frequency Control. This is the author's version which has not been fully edited an content may change prior to final publication. Citation information: DOI 10.1109/TUFFC.2021.3076284

8

TABLE IV *PW TRANSMISSION BY LINEAR ARRAY WITH UNFOCUSED LENS: RELATIVE BIAS AND MEAN STANDARD DEVIATION OF VELOCITY ESTIMATES BY 2-D VECTOR FLOW IMAGING*

Depth [mm]	Flat profile $\overline{B}_{v_{Module}} \pm \overline{\sigma}_{v_{Module}}$ [%]			Parabolic profile $\overline{B}_{v_{Module}} \pm \overline{\sigma}_{v_{Module}}$ [%]		
	$\vartheta_D = 90°$	$\vartheta_D = 82.5°$	$\vartheta_D = 75°$	$\vartheta_D = 90°$	$\vartheta_D = 82.5°$	$\vartheta_D = 75°$
20	-3.8±2.4	-4.2±2.7	-4.6±3.9	-12.8±3	-13.5±4.7	-13.6±6.6
40	-4.3±2.6	-4.8±2.9	-4.8±3.5	-10.6±3.1	-9.6±4.2	-10.8±6.6
60	-4.4±2.7	-5±2.9	-4.8±3.7	-8.3±2.8	-9.8±4.2	-10±5.8
80	-9.1±3	-9.5±3.2	-9.7±3.6	-11.6±3	-11.7±4.4	-11.8±5.7
100	-17.4±3.1	-16.9±3.2	-15.8±4.6	-18.9±3.7	-19.9±4.9	-19.4±7.7

REFERENCES

[1] D. H. Evans and W. N. McDicken, *Doppler Ultrasound: Physics, Instrumentation and Signal Processing*, 2nd Edition. Wiley-Blackwell, 1999.

[2] P. Tortoli, G. Guidi, P. Berti, F. Guidi, and D. Righi, "An FFT-based flow profiler for high-resolution in vivo investigations," *Ultrasound Med. Biol.*, vol. 23, no. 6, pp. 899–910, 1997, doi: 10.1016/S0301-5629(97)00017-3.

[3] P. Tortoli, F. Guidi, G. Guidi, and C. Atzeni, "Spectral velocity profiles for detailed ultrasound flow analysis," *IEEE Trans. Ultrason. Ferroelectr. Freq. Control*, vol. 43, no. 4, pp. 654–659, Jul. 1996, doi: 10.1109/58.503727.

[4] M. D. Fox, "Multiple crossed-beam ultrasound Doppler velocimetry," *IEEE Trans. Sonics Ultrason.*, vol. 25, no. 5, pp. 281–286, Sep. 1978, doi: 10.1109/T-SU.1978.31028.

[5] B. Dunmire, K. W. Beach, K.-H. Labs, M. Plett, and D. E. Strandness Jr., "Cross-beam vector Doppler ultrasound for angle-independent velocity measurements," *Ultrasound Med. Biol.*, vol. 26, no. 8, pp. 1213–1235, Oct. 2000, doi: 10.1016/S0301-5629(00)00287-8.

[6] R. Steel, K. V. Ramnarine, F. Davidson, P. J. Fish, and P. R. Hoskins, "Angle-independent estimation of maximum velocity through stenoses using vector Doppler ultrasound," *Ultrasound Med. Biol.*, vol. 29, no. 4, pp. 575–584, Apr. 2003, doi: 10.1016/S0301-5629(02)00736-6.

[7] P. Tortoli, A. Dallai, E. Boni, L. Francalanci, and S. Ricci, "An Automatic Angle Tracking Procedure for Feasible Vector Doppler Blood Velocity Measurements," *Ultrasound Med. Biol.*, vol. 36, no. 3, pp. 488–496, Mar. 2010, doi: 10.1016/j.ultrasmedbio.2009.11.004.

[8] J. A. Jensen and P. Munk, "A new method for estimation of velocity vectors," *IEEE Trans. Ultrason. Ferroelectr. Freq. Control*, vol. 45, no. 3, pp. 837–851, May 1998, doi: 10.1109/58.677749.

[9] S. Ricci, L. Bassi, and P. Tortoli, "Real-time vector velocity assessment through multigate Doppler and plane waves," *IEEE Trans. Ultrason. Ferroelectr. Freq. Control*, vol. 61, no. 2, pp. 314–324, Feb. 2014, doi: 10.1109/TUFFC.2014.6722616.

[10] L. N. Bohs, B. H. Friemel, and G. E. Trahey, "Experimental velocity profiles and volumetric flow via two-dimensional speckle tracking," *Ultrasound Med. Biol.*, vol. 21, no. 7, pp. 885–898, Jan. 1995, doi: 10.1016/0301-5629(95)00034-O.

[11] J. Udesen, M. B. Nielsen, K. R. Nielsen, and J. A. Jensen, "Examples of In Vivo Blood Vector Velocity Estimation," *Ultrasound Med. Biol.*, vol. 33, no. 4, pp. 541–548, Apr. 2007, doi: 10.1016/j.ultrasmedbio.2006.10.014.

[12] K. L. Hansen *et al.*, "In vivo comparison of three ultrasound vector velocity techniques to MR phase contrast angiography," *Ultrasonics*, vol. 49, no. 8, pp. 659–667, Dec. 2009, doi: 10.1016/j.ultras.2009.04.002.

[13] J.-Y. Lu, "2D and 3D high frame rate imaging with limited diffraction beams," *IEEE Trans. Ultrason. Ferroelectr. Freq. Control*, vol. 44, no. 4, pp. 839–856, Jul. 1997, doi: 10.1109/58.655200.

[14] S. I. Nikolov and J. A. Jensen, "Velocity estimation using synthetic aperture imaging [blood flow]," in *2001 IEEE Ultrasonics Symposium. Proceedings. An International Symposium (Cat. No.01CH37263)*, Oct. 2001, vol. 2, pp. 1409–1412 vol.2, doi: 10.1109/ULTSYM.2001.991985.

[15] J. Cheng and J.-Y. Lu, "Extended high-frame rate imaging method with limited-diffraction beams," *IEEE Trans. Ultrason. Ferroelectr. Freq. Control*, vol. 53, no. 5, pp. 880–899, May 2006, doi: 10.1109/TUFFC.2006.1632680.
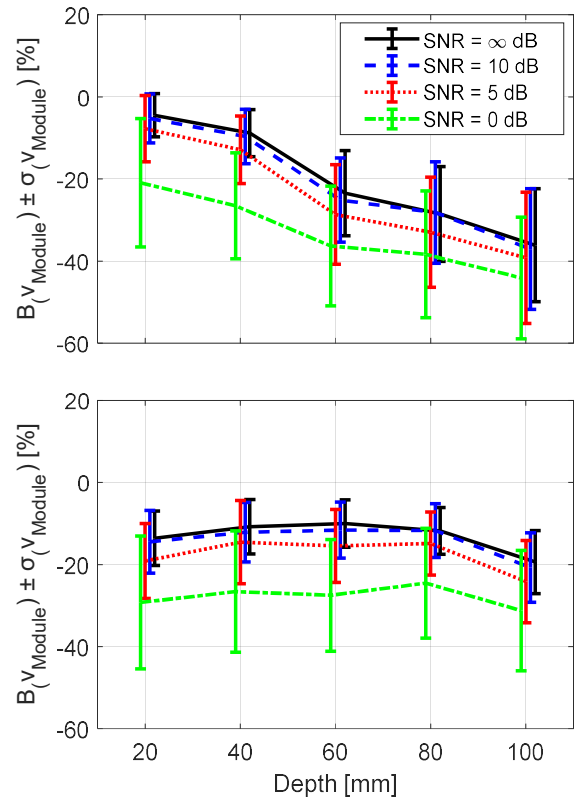
Fig. A1 Relative bias and standard deviaton of (2-D VFI) velocity estimates obtained by the linear array with (top) and without (bottom) the focused lens. In this example, ϑ_D was 75°, the flow had a parabolic profile, and four different SNRs (∞, 10, 5, 0 dB) were considered.

[16] G. Montaldo, M. Tanter, J. Bercoff, N. Benech, and M. Fink, "Coherent plane-wave compounding for very high frame rate ultrasonography and transient elastography," *IEEE Trans. Ultrason. Ferroelectr. Freq. Control*, vol. 56, no. 3, pp. 489–506, Mar. 2009, doi: 10.1109/TUFFC.2009.1067.

[17] C. Papadacci, M. Pernot, M. Couade, M. Fink, and M. Tanter, "High-contrast ultrafast imaging of the heart," *IEEE Trans. Ultrason. Ferroelectr. Freq. Control*, vol. 61, no. 2, pp. 288–301, Feb. 2014, doi: 10.1109/TUFFC.2014.6722614.

[18] H. Hasegawa and H. Kanai, "High-frame-rate echocardiography using diverging transmit beams and parallel receive beamforming," *J. Med. Ultrason.*, vol. 38, no. 3, Art. no. 3, May 2011, doi: 10.1007/s10396-011-0304-0.

[19] N. Ghigo, A. Ramalli, S. Ricci, P. Tortoli, D. Vray, and H. Liebgott, "Sequence optimization for high frame rate imaging with a convex array," in *2020 IEEE International Ultrasonics Symposium (IUS)*, Sep. 2020, pp. 1–4, doi: 10.1109/IUS46767.2020.9251286.

[20] S. Fadnes, M. S. Wigen, S. A. Nyrnes, and L. Lovstakken, "In Vivo Intracardiac Vector Flow Imaging Using Phased Array Transducers for Pediatric Cardiology," *IEEE Trans. Ultrason. Ferroelectr. Freq. Control*, vol. 64, no. 9, pp. 1318–1326, Sep. 2017, doi: 10.1109/TUFFC.2017.2689799.

[21] J. Faurie *et al.*, "Intracardiac Vortex Dynamics by High-Frame-Rate Doppler Vortography—In Vivo Comparison With Vector Flow Mapping and 4-D Flow MRI," *IEEE Trans. Ultrason. Ferroelectr. Freq. Control*, vol. 64, no. 2, pp. 424–432, Feb. 2017, doi: 10.1109/TUFFC.2016.2632707.

[22] N. Ghigo *et al.*, "High Frame Rate Vector Flow Imaging with a Convex Array in a simulated vessel phantom," in *2019 IEEE International Ultrasonics Symposium (IUS)*, Oct. 2019, pp. 356–359, doi: 10.1109/ULTSYM.2019.8925612.

[23] A. Besson, F. Wintzenrieth, and C. Cohen-Bacrie, "Vector-flow Imaging in Convex-array Configurations," in *2020 IEEE International Ultrasonics Symposium (IUS)*, Sep. 2020, pp. 1–4, doi: 10.1109/IUS46767.2020.9251541.

[24] S. A. Nyrnes, S. Fadnes, M. S. Wigen, L. Mertens, and L. Lovstakken, "Blood Speckle-Tracking Based on High–Frame Rate Ultrasound Imaging in Pediatric Cardiology," *J. Am. Soc. Echocardiogr.*, vol. 33, no. 4, pp. 493-503.e5, Apr. 2020, doi: 10.1016/j.echo.2019.11.003.

This article has been accepted for publication in IEEE Transactions on Ultrasonics, Ferroelectrics, and Frequency Control. This is the author's version which has not been fully edited and content may change prior to final publication. Citation information: DOI 10.1109/TUFFC.2021.3076284

9

[25] V. Perrot *et al.*, "Translation of Simultaneous Vessel Wall Motion and Vectorial Blood Flow Imaging in Healthy and Diseased Carotids to the Clinic: a Pilot Study," *IEEE Trans. Ultrason. Ferroelectr. Freq. Control*, pp. 1–1, 2020, doi: 10.1109/TUFFC.2020.3015340.

[26] J. A. Jensen, H. Liebgott, F. Cervenansky, and C. A. Villagomez Hoyos, "SA-VFI: the IEEE IUS Challenge on Synthetic Aperture Vector Flow Imaging," in *2018 IEEE International Ultrasonics Symposium (IUS)*, Kobe, Oct. 2018, pp. 1–5, doi: 10.1109/ULTSYM.2018.8580208.

[27] S. Fadnes, I. K. Ekroll, S. A. Nyrnes, H. Torp, and L. Lovstakken, "Robust angle-independent blood velocity estimation based on dual-angle plane wave imaging," *IEEE Trans. Ultrason. Ferroelectr. Freq. Control*, vol. 62, no. 10, pp. 1757–1767, Oct. 2015, doi: 10.1109/TUFFC.2015.007108.

[28] B. Y. S. Yiu and A. C. H. Yu, "Least-Squares Multi-Angle Doppler Estimators for Plane-Wave Vector Flow Imaging," *IEEE Trans. Ultrason. Ferroelectr. Freq. Control*, vol. 63, no. 11, pp. 1733–1744, Nov. 2016, doi: 10.1109/TUFFC.2016.2582514.

[29] S. Ricci, A. Ramalli, L. Bassi, E. Boni, and P. Tortoli, "Real-Time Blood Velocity Vector Measurement Over a 2-D Region," *IEEE Trans. Ultrason. Ferroelectr. Freq. Control*, vol. 65, no. 2, pp. 201–209, Feb. 2018, doi: 10.1109/TUFFC.2017.2781715.

[30] R. Steel and P. J. Fish, "Velocity bias and fluctuation in the standard dual beam Doppler reconstruction algorithm," *IEEE Trans. Ultrason. Ferroelectr. Freq. Control*, vol. 49, no. 10, pp. 1375–1383, Oct. 2002, doi: 10.1109/TUFFC.2002.1041079.

[31] G. E. Trahey, J. W. Allison, and O. T. von Ramm, "Angle Independent Ultrasonic Detection of Blood Flow," *IEEE Trans. Biomed. Eng.*, vol. BME-34, no. 12, pp. 965–967, Dec. 1987, doi: 10.1109/TBME.1987.325938.

[32] L. N. Bohs, B. J. Geiman, M. E. Anderson, S. C. Gebhart, and G. E. Trahey, "Speckle tracking for multi-dimensional flow estimation," *Ultrasonics*, vol. 38, no. 1–8, pp. 369–375, Mar. 2000.

[33] J. Udesen, F. Gran, K. L. Hansen, J. A. Jensen, C. Thomsen, and M. B. Nielsen, "High frame-rate blood vector velocity imaging using plane waves: simulations and preliminary experiments," *IEEE Trans. Ultrason. Ferroelectr. Freq. Control*, vol. 55, no. 8, Art. no. 8, Aug. 2008, doi: 10.1109/TUFFC.2008.858.

[34] M. Lenge, A. Ramalli, E. Boni, H. Liebgott, C. Cachard, and P. Tortoli, "High-frame-rate 2-D vector blood flow imaging in the frequency domain,"

IEEE Trans. Ultrason. Ferroelectr. Freq. Control, vol. 61, no. 9, pp. 1504–1514, Sep. 2014, doi: 10.1109/TUFFC.2014.3064.

[35] M. Lenge, A. Ramalli, P. Tortoli, C. Cachard, and H. Liebgott, "Plane-wave transverse oscillation for high-frame-rate 2-D vector flow imaging," *IEEE Trans. Ultrason. Ferroelectr. Freq. Control*, vol. 62, no. 12, pp. 2126–2137, Dec. 2015, doi: 10.1109/TUFFC.2015.007320.

[36] J. A. Jensen, S. I. Nikolov, A. C. H. Yu, and D. Garcia, "Ultrasound Vector Flow Imaging - Part II: Parallel Systems," *IEEE Trans. Ultrason. Ferroelectr. Freq. Control*, vol. 63, no. 11, pp. 1722–1732, Nov. 2016, doi: 10.1109/TUFFC.2016.2598180.

[37] S. Rossi *et al.*, "Performance of Ultrasound Vector Velocity Measurement at Great Depths," in *2019 IEEE International Ultrasonics Symposium (IUS)*, Glasgow, United Kingdom, Oct. 2019, pp. 368–371, doi: 10.1109/ULTSYM.2019.8925547.

[38] S. Rossi, A. Ramalli, L. Francalanci, and P. Tortoli, "Influence of the Acoustic Lens on Vector Doppler Measurements Based on Plane Wave Transmission: a Simulation Study," in *2020 IEEE International Ultrasonics Symposium (IUS)*, Las Vegas, NV, USA, Sep. 2020, pp. 1–3, doi: 10.1109/IUS46767.2020.9251427.

[39] J. A. Jensen, "A multi-threaded version of Field II," in *2014 IEEE International Ultrasonics Symposium*, Chicago, IL, USA, Sep. 2014, pp. 2229–2232, doi: 10.1109/ULTSYM.2014.0555.

[40] J. Provost, C. Papadacci, C. Demene, J. L. Gennisson, M. Tanter, and M. Pernot, "3-D ultrafast doppler imaging applied to the noninvasive mapping of blood vessels in Vivo," *IEEE Trans. Ultrason. Ferroelectr. Freq. Control*, vol. 62, no. 8, pp. 1467–1472, Aug. 2015, doi: 10.1109/TUFFC.2015.007032.

[41] S. Holbek, T. L. Christiansen, M. B. Stuart, C. Beers, E. V. Thomsen, and J. A. Jensen, "3-D Vector Flow Estimation With Row–Column-Addressed Arrays," *IEEE Trans. Ultrason. Ferroelectr. Freq. Control*, vol. 63, no. 11, pp. 1799–1814, Nov. 2016, doi: 10.1109/TUFFC.2016.2582536.

[42] M. S. Wigen *et al.*, "4-D Intracardiac Ultrasound Vector Flow Imaging–Feasibility and Comparison to Phase-Contrast MRI," *IEEE Trans. Med. Imaging*, vol. 37, no. 12, pp. 2619–2629, Dec. 2018, doi: 10.1109/TMI.2018.2844552.

[43] S. Rossi, A. Ramalli, F. Fool, and P. Tortoli, "High-Frame-Rate 3-D Vector Flow Imaging in the Frequency Domain," *Appl. Sci.*, vol. 10, no. 15, p. 5365, Aug. 2020, doi: 10.3390/app10155365.